Pattern formation during deformation of metallic nanolaminates

Adrien Gola,[1,2] Ruth Schwaiger,[2,3,4] Peter Gumbsch,[2,5] and Lars Pastewka[1,6,7,*]

[1]*Department of Microsystems Engineering, University of Freiburg, Georges-Köhler-Allee 103, 79110 Freiburg, Germany*
[2]*Institute for Applied Materials, Karlsruhe Institute of Technology, Kaiserstraße 12, 76131 Karlsruhe, Germany*
[3]*Institute of Energy and Climate Research (IEK-2), Forschungszentrum Juelich GmbH, 52425 Juelich, Germany*
[4]*Chair of Energy Engineering Materials, RWTH Aachen University, 52056 Aachen, Germany*
[5]*Fraunhofer IWM, Wöhlerstraße 11, 79108 Freiburg, Germany*
[6]*Freiburg Materials Research Center, University of Freiburg, Stefan-Meier-Straße 21, 79104 Freiburg, Germany*
[7]*Cluster of Excellence livMatS, Freiburg Center for Interactive Materials and Bioinspired Technologies, University of Freiburg, Georges-Köhler-Allee 105, 79110 Freiburg, Germany*

(Received 30 June 2019; revised manuscript received 29 November 2019; published 10 January 2020)

We used nonequilibrium molecular dynamics simulations to study the shear deformation of metallic composites composed of alternating layers of Cu and Au. Our simulations reveal the formation of "vortices" or "swirls" if the bimaterial interfaces are atomically rough and if none of the {111} planes that accommodate slip in fcc materials are exactly parallel to this interface. We trace the formation of these patterns back to grain rotation, induced by hindering dislocations from crossing the bimaterial interface. The instability is accompanied by shear softening of the material. These calculations shed light on recent observations of pattern formation in plastic flow, mechanical mixing of materials, and the common formation of a tribomutation layer in tribologically loaded systems.

DOI: 10.1103/PhysRevMaterials.4.013603

I. INTRODUCTION

Nanolaminates or multilayers are layered composites, consisting of planar layers of alternating composition with thickness on the order of nanometers to hundreds of nanometers. They have attracted interest over the past decades for their excellent mechanical properties such as high strength and wear resistance [1–3]. In addition, nanolaminates are interesting model systems because the full deformation field can be extracted in experiments simply by tracing the layer structure *postmortem*.

Significant plastic deformation takes place when indenting or scratching a surface [4]. Indeed, plastic deformation is responsible for part of the material loss during abrasive [5] and sliding wear [6]. The plowing motion of asperities on the counterbody contributes to the friction between two materials [6–8]. Nanolaminates allow the tracing of the subsurface deformation through the lifetime of a frictional contact, which may reveal the contribution of plasticity to these processes.

Recently, Luo *et al.* [9] have experimentally observed intermixing of individual layers during reciprocating sliding. Their experiments on Cu|Au nanolaminates with 100-nm-thick layers show interface roughening during the early stages of cycling, followed by vortex formation and intermixing [see Figs. 1(a)–1(c)]. Cihan *et al.* [10] observed similar vortices for layer thicknesses varying from 10 to 50 nm in Au|Ni nanolaminates. While Cu-Au is miscible, Au-Ni is an immiscible metallic system. Both show the formation of vortices, which indicates that vortices and mechanical alloying are related phenomena. Indeed, early molecular dynamics (MD) simulations also showed the formation of vortices of a few atomic distances in size at the sliding contact between metallic crystalline [11,12] or amorphous [13–15] bodies. The vortices in those calculations drove chemical mixing [16–19] and were a consequence of shear localization. Direct experimental observation of such vortices had proven difficult but is now possible in metallic nanolaminates where the deformation field is visible at the bimaterial interfaces [Figs. 1(a)–1(c)]. The "vortices" or "swirls" occurring at the interface are reminiscent of similar patterns observed, for example, during the formation of clouds, from fluid instabilities such as the one named after Lord Kelvin and von Helmholtz [20,21]. These Kelvin-Helmholtz instabilities occur in the turbulent regime of fluids, i.e., at large Reynolds numbers [22].

More recently, Pouryazdan *et al.* [23] observed similar vortices in high-pressure torsion experiments of alternatingly stacked Cu|Al foils of 25 μm in thickness, which were much thicker than the Cu|Au nanolaminates of Luo *et al.* [9]. Pouryazdan *et al.* [23] pointed out that the velocities required to be in a turbulent regime at the contact of two metallic crystals were unrealistically high (hundreds of km s^{-1}). The Kelvin-Helmholtz instabilities are therefore unlikely to occur in such composites. Pouryazdan *et al.* [23] proposed an alternative fluid-mechanical model, a layered composite with layers of different viscosities, to demonstrate the formation of vortices at the interface of the two viscous fluids. While the proposed model did not involve unrealistic flow velocities, it required unidirectional strains up to 400 for the vortices to fully develop. Such extremely high applied strains are easily achievable by high-pressure torsion as the shear strain scales linearly with the sample diameter and the number of

*lars.pastewka@imtek.uni-freiburg.de

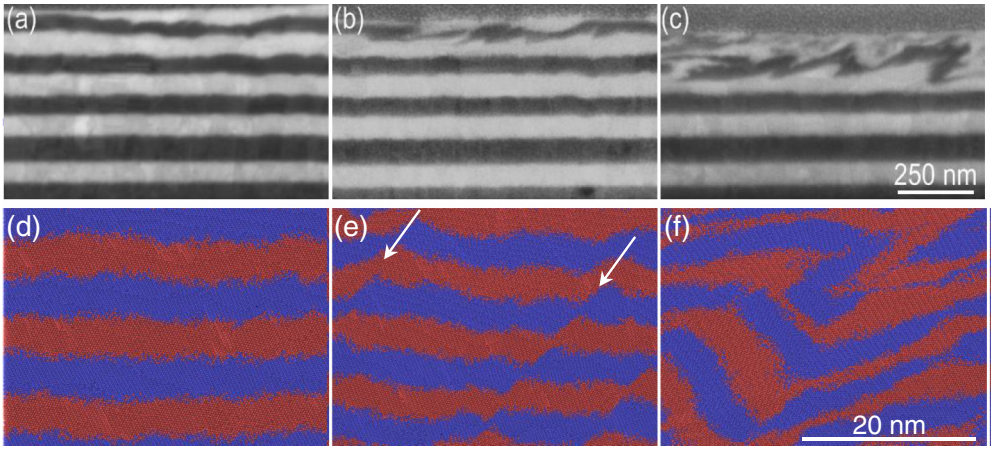

FIG. 1. (a–c) SEM images (at 52° sample tilt) of cross sections of Cu|Au nanolaminates of 100-nm layer thickness during cyclic sliding with a spherical diamond tip of 16.7 μm in diameter. Snapshots are obtained after (a) 10, (b) 20, and (c) 100 sliding cycles. For more details on the experimental procedure see Luo *et al.* [9]. (d–f) Snapshots of the molecular dynamics simulation of the nanolaminate with surface planes misoriented by $\theta = 5^\circ$ with respect to the (111) direction. Snapshots are shown (d) during equibiaxial deformation along the x and y axis at an applied strain of ε_{xx}, $\varepsilon_{yy} = 0.12$, (e) after equibiaxial deformation to an applied strain of ε_{xx}, $\varepsilon_{yy} = 0.25$, and (f) after subsequent simple shear deformation to an applied strain of $\varepsilon_{xz} = 3.0$.

revolutions. However, these strains are much larger than those achieved under a sliding track [9].

The mechanism responsible for the formation of patterns such as those shown in Fig. 1 remains unclear. Vortices at atomic scales that led to mechanical mixing in previous MD simulations were much smaller than the patterns shown in Fig. 1 that are clearly on an intermediate scale—that of the thickness of the individual layers. A purely fluid-mechanical explanation would require unrealistic velocities or extraordinarily large unidirectional strains, although the cumulative strain after multiple reciprocating passes of a sliding body may be large. An alternative mechanism for the formation of vortex structures in nanolaminates must therefore be active. We investigated the phenomenon of vortex formation using nonequilibrium MD calculations of deformation of Cu|Au nanolaminates.

Understanding the deformation process can yield insights into tribomaterial formation processes [12] that occur in almost all tribological contacts, where the near-surface material transforms—e.g., by grain refinement, [24,25] or amorphization [26–28].

II. SIMULATION MODEL AND METHODS

Our simulations are designed to uncover the conditions required for inducing vortex instabilities. Since we know the conditions under which they are observed experimentally, our simulation model is guided by the experiments of Luo *et al.* [9] on Cu|Au nanolaminates. The experiments used a spherical indenter of radius R much larger than the layer thickness λ, $\lambda/R = 6 \times 10^{-3}$, in Ref. [9]. The stress field is roughly homogeneous on the scale of the layer thickness λ and we only regard representative volume elements subjected to strain-controlled deformation. (See Fig. 2; a structural mechanical model on the full scale of the experiment is out of reach on present-day computers within molecular simulations.) The representative volume element used in this work is shown in Fig. 2(c). Due to the film growth process, the surface normal of the bimaterial interface is always close to a {111} plane. Our calculations also allow the possibility of having a slight misorientation (angle θ) between the crystallographic direction and the bimaterial interface [see inset of Fig. 2(c)]. Note that this is not a misorientation between the Cu and Au layers, but between the lattice orientation of both Cu and Au and the interface separating them. A residual misorientation between the lattices of Cu and Au remains only because of constraints on tilt angles imposed by the periodic boundary conditions (see Table I).

The initial system shown in Fig. 2(c) is composed of 10 layers of 5-nm thickness each, with an in-plane size of approximately 30×30 nm^2. We also investigated possible size effects by running a similar calculation on a "supercell" system nine times larger comprised of 30 layers obtained by replicating the undeformed system cell in the x and z

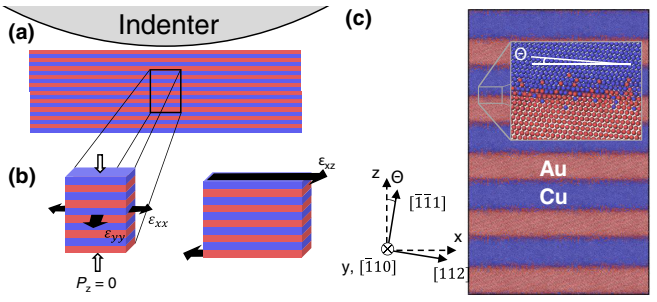

FIG. 2. (a) Schematic representation of the experimental setup similar to the one described in Luo *et al.* [9]. (b) Schematic representation of the two deformation steps applied to the representative volume element used in our simulations. (c) Snapshot of the initial simulation setup. The inset shows the misalignment of the lattice. The angle relative to a perfect (111) orientation is denoted by θ. We use a right-hand coordinate system, with the sliding direction chosen as x.

TABLE I. Minimum simulation cell size used for our simulations. The numbers n and m denote the number of unit cells of the Au and Cu layers, respectively. A ratio of $m/n \neq 1$ and different tilt angles θ are necessary to accommodate the nominal lattice mismatch and comply with the periodic boundary conditions. All systems are composed of 10 layers, with the exception of the system denoted by supercell that contained 30 layers.

Setup name	θ_{Au}/θ_{Cu} (°)	$n_{[112]}/m_{[112]}$	$n_{[\bar{1}10]}/m_{[\bar{1}10]}$
0°	0/0	66/74	125/140
2.5°	2.45/2.19	66/74	125/140
5°	4.90/4.37	66/74	125/140
5° (supercell)	4.90/4.37	198/222	125/140
10°	10.0/8.93	64/72	125/140

directions for $\theta = 5°$. Table I gives the exact number of Au and Cu unit cells used in the in-plane directions and the corresponding tilt angles. We used periodic boundary conditions in all directions.

We created the initial configuration from ideal Cu and Au fcc slabs with intermixed interfaces. Since Cu and Au are miscible (and can even form stable binary phases) [29–31], the interfaces between Cu and Au were intermixed to mimic the interdiffusion observed in high-resolution microscopy of these multilayers [32]. We mixed the interface region by randomly flipping Cu and Au atoms over a finite interface width of 15 Å, such that the final concentration profile follows the error function predicted by simple Fickian interdiffusion [33]. Note that interdiffusion of the interfaces is necessary to reproduce the experimental values for the interfacial shear strength of this material (see the supplementary materials of Ref. [34]).

For the molecular simulation of the binary Cu-Au system, we used an embedded atom method potential. The potential is based on two high-quality potentials for the pure Cu and Au phases [35,36]. These potentials provide an excellent description of the stacking fault energy of the unary phases, which is crucial for the proper prediction of mechanical properties of our structures. All binary Cu-Au potentials underestimate these stacking fault energies by around an order of magnitude. We therefore tailored a cross potential between the unary potentials of Mishin *et al.* [35] and Grochola *et al.* [36] to the properties of the Cu_3Au, CuAu, and $CuAu_3$ phases. A detailed description of the potential and its properties, including a computation of its phase diagram, can be found in Ref. [37].

The systems were annealed at 1000 K for a total of 2 ns in MD and then quenched down to 300 K at a rate of 350 K ns^{-1}. This was followed by further aging the system at 300 K for 1 ns. During these annealing simulations, the temperature of the whole system was controlled using a Langevin thermostat with a relaxation time of 1 ps. We used an anisotropic Berendsen barostat [38] with a relaxation time of ∼5 ps to maintain zero stress along the [112] and [110] directions. All calculation steps were performed with a time step of 5 fs.

We replicated the system along the z axis to obtain the final 10 layers as shown in Fig. 2. The systems then underwent two successive deformation steps: equibiaxial tensile deformation up to a biaxial strain of 25% followed by simple shear [see Fig. 2(b)]. All deformation simulations were carried out at 300 K with a strain rate of 10^8 s^{-1}. The temperature of the whole system was controlled using a Nosé-Hoover thermostat with a relaxation time of 1 ps. For simple shear deformation the thermostat is applied only in the direction perpendicular to the shearing direction. The equibiaxial tensile deformation was imposed by changing the simulation box size along the x and y directions according to the defined strain rate. The pressure perpendicular to the deformation (i.e., z direction) was kept at zero using the Andersen–Parinello-Rahman barostat [39,40] with a relaxation time constant of 10 ps. Simple shear deformation was then applied along the interface planes, i.e., along $[112](\bar{1}\bar{1}1)$ for $\theta = 0°$, by homogeneously deforming the box at the prescribed strain rate. Our notation $[abc](hkl)$ for simple shear reports both the direction of shear $[abc]$ and the plane of shear (hkl).

During shear, we quantified the lattice orientation of local regions within our simulation. The lattice orientation was obtained using polyhedral template matching [41,42]. We determined the orientation along the z axis (multilayer growth axis) and used an equal-area projection to assign a color to each atom. We also quantified elastic and plastic rearrangements rather than defects by computing the local strain tensor from the analysis of Falk and Langer [43] within local neighbor spheres of a radius that include just an atom's nearest neighbors. This technique computes the atomic neighborhood in a reference frame and then extracts the deformation gradient tensor $\mathbf{F}_i$ necessary to transform the vectors connecting the atom i of interest to its reference neighborhood to the deformed configuration in a least-squares sense. Then from the deformation gradient the local Green-Lagrangian strain tensor is computed [44], $\boldsymbol{\gamma}_i = (\mathbf{F}_i^T \mathbf{F}_i - \mathbf{I})/2$. With this method one can visualize the total amount of local deformation a system has experienced, i.e., where dislocations have passed.

III. RESULTS

Equibiaxial deformation. The initial systems with 10 layers and misalignment ranging from $\theta = 0°$ to 10° with interfaces parallel to the x-y plane were deformed by equibiaxial deformation along the x and y axes [see Fig. 2(b)]. Each atom was assigned to a single layer l at the beginning of the calculation and this assignment stayed fixed during the course of the calculation. We characterize the thickness of each layer by its root mean square width,

$$w^l_{\mathrm{RMS}}(t) = \sqrt{\frac{1}{N_l}\sum_{i\in l}\left(z_i(t) - \frac{1}{N_l}\sum_{j\in l} z_j(t)\right)^2}, \qquad (1)$$

with the total number of atoms in this layer, N_l, and the z component of atom i at time step t, $z_i(t)$. Figure 3(a) shows the evolution of the average w^l_{RMS}, averaged over Cu and Au layers l separately.

This measure allows us to track layer thinning and broadening. During the equibiaxial deformation, w_{RMS} showed a similar behavior for all the systems independent of their misorientation. w_{RMS} monotonically decreased until it reached a minimum at a strain of approximately 20% before slightly

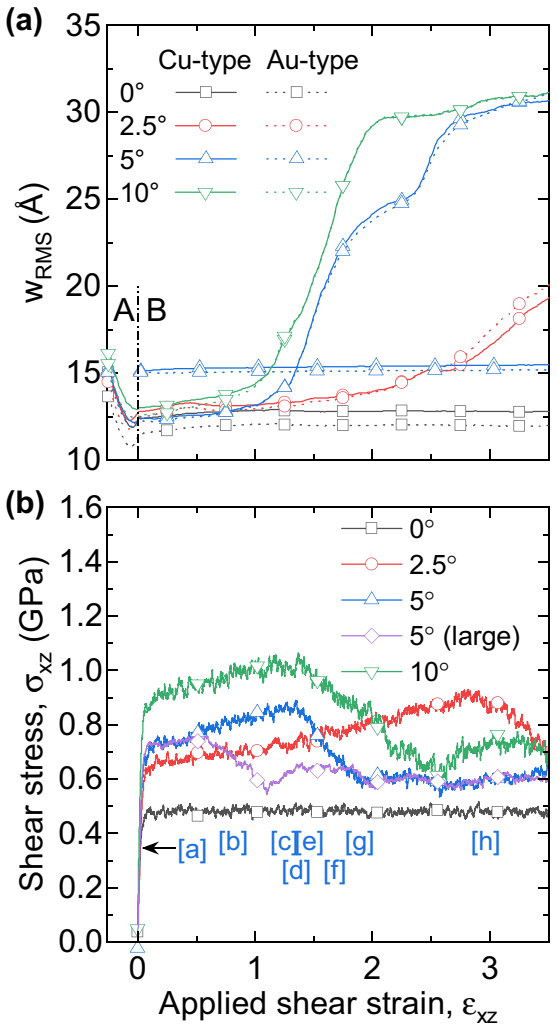

FIG. 3. (a) Averaged root mean square of the layer width, w^l_{RMS} [Eq. (1)], over the course of the biaxial (subplot A) and simple shear deformation (subplot B). (b) Stress-strain curves obtained during the simple shear calculation of the misoriented {111} planes for $\theta = 0°$, 2.5°, 5°, and 10°. The blue letters in square brackets indicate the strain values corresponding to the snapshots shown in Fig. 5 for the $\theta = 5°$ calculation.

increasing towards the final applied strain of 25%. Both Cu-type and Au-type layers thinned down at the same rate.

Figures 1(e) (lattice tilt of $\theta = 5°$) and 4(a) ($\theta = 0°$) show snapshots of the systems after equibiaxial deformation at 25% strain. From these images it is clear that the initially straight interfaces roughened during deformation. Both $\theta = 5°$ and 0° systems developed shear bands that crossed several layers, creating the most pronounced roughness features at the interfaces (shown by white arrows in the corresponding figures).

Simple shear deformation. After equibiaxial deformation, the systems were deformed by applying simple shear. Figure 3(b) shows the stress-strain curves obtained for the four systems of interest. The system without misorientation ($\theta = 0°$) showed a flat stress-strain curve. This behavior is identical to the one observed for simple shear deformation of a perfectly flat Cu|Au bilayer sheared parallel to the interface (see supporting material of Ref. [34]). After the initial elastic response, both systems yielded at around 0.5 GPa and then entered a flow regime with a flow stress fluctuating around this value. For flat interfaces, an analysis of the local strain rate [43] revealed that all of the strain is accommodated at the bilayer interfaces.

The stress required to deform the systems with misorientation of the {111} planes increased with increasing θ. The nanolaminates yielded between 0.6 GPa for $\theta = 2.5°$ and 0.88 GPa for $\theta = 10°$. All misoriented systems then showed strain hardening, manifested in an almost linear stress-strain relationship. During hardening, the systems encountered an instability. The shear stress started to drop at $\sigma \approx 0.9$ GPa (at an applied strain of $\varepsilon \approx 2.9$) for $\theta = 2.5°$, $\sigma \approx 0.9$ GPa ($\varepsilon \approx 1.3$) for $\theta = 5°$, and $\sigma \approx 1.0$ GPa ($\varepsilon \approx 1.3$) for $\theta = 10°$. The shear stress eventually dropped to roughly the same value of 0.6 GPa for all the systems. The systems continued to shear at that stress during subsequent deformation. Again, analysis of the local strain rate showed that strain was accommodated at localized regions oriented parallel to the simulation cell boundary once the instability had occurred.

Figure 3(a) shows that the point of the instability (the stress drop) for the misoriented systems coincided with the rapid increase of w_{RMS}, while for $\theta = 0°$ (no instability), w_{RMS} stayed constant during the whole shear deformation. Figure 1(f) shows a snapshot of the system with $\theta = 5°$ sheared to an applied strain of $\varepsilon = 3.0$. For $\theta = 5°$, the

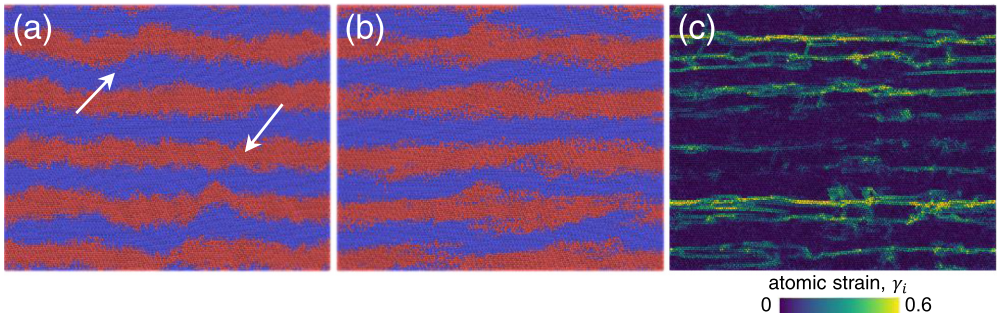

FIG. 4. Snapshots of the nanolaminate stack with $[\bar{1}\bar{1}1]$ planes initially aligned with the interfaces. Snapshot taken (a) after equibiaxial deformation along the x and y axis to $\varepsilon_{xx} = \varepsilon_{yy} = 0.25$ and (b,c) after subsequent simple shear deformation to $\varepsilon_{xz} = 3.0$. Atoms in panels (a) and (b) are colored according to their type; Cu atoms are in blue and Au atoms in red. Atoms in panel (c) are colored after their local atomic shear strain γ_i. The atomic strains are computed based on a reference system at an applied strain of $\varepsilon_{xz} = 2.9$.

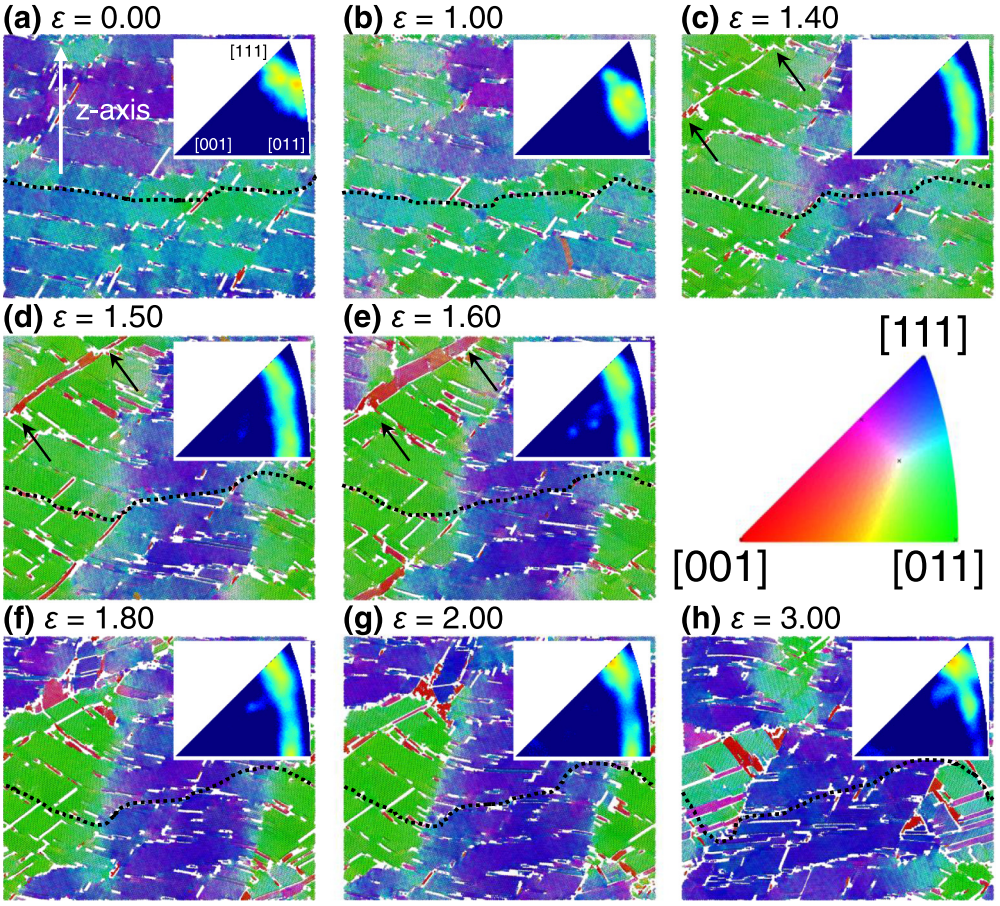

FIG. 5. Orientation maps of the system with a misorientation of $\theta = 5^\circ$ during simple shear deformation as a sequence from (a) the initial configuration at zero strain to (h) an applied strain of three. The panels (a–h) show snapshots for the points marked [a–h] in Fig. 3(c). Non-fcc atoms have been removed, fcc atoms are color coded after their local lattice orientations along the z axis. The interfaces are less visible with this color scheme; for clarity one interface is marked up with a black dashed line. The arrows in panel (c) indicate the boundaries of the twinning event. The insets show inverse pole figures with the local lattice orientation density along the z axis of the simulation cell in the standard stereographic triangle. The color coding used here follows a jet colormap with high pole density in red and low density in blue.

layered structure is severely deformed with noticeable patterns, similar to the experimental "vortices" shown in Fig. 1(c). Without misorientation ($\theta = 0^\circ$) the deformation is accommodated along the interfaces and the bimaterial interfaces remain straight [see Figs. 4(b) and 4(c)].

In order to gain more insights into the mechanism underlying the observed instability and the formation of the vortexlike patterns, we now focus on the system with a misorientation of $\theta = 5^\circ$ and describe in detail the deformation process. Figure 5 shows snapshots of the system. The atoms are color-coded according to their local lattice orientation in the direction of the z-axis (normal to the initial bilayer interfaces). Atoms that are not in a local fcc environment (and hence cannot be assigned an orientation) are not shown. The insets in Fig. 5 show inverse pole figures of the distribution of these local lattice orientations found throughout the simulation cell.

Before shear there were two main orientations in the system [Fig. 5(a)], colored by purple and green, corresponding to orientations of the z axis approximately along the [432] and [553] directions, respectively. Note that the transition between these two regions roughly corresponds to the location of the shear bands seen in Fig. 1(e). At a shear strain of $\varepsilon = 1.4$, i.e., right after the stress drops, we can see traces of dislocations that cross three layers, marked by the two black arrows in Fig. 5(c). At this point we also observe a significant rotation of the local lattice toward the [011] direction, leading to a broad band of orientations in the inverse pole figure [inset to Fig. 5(c)]. At $\varepsilon = 1.6$, this interlayer region has widened (marked with two black arrows). We now have in the system the presence of a large twinned area [red in Figs. 5(c)–5(e), marked by two black arrows].

At an applied strain of $\varepsilon = 1.8$ and above, this zone shrank as part of the lattice rotated back to a (111) orientation. This rotation led to the creation of two misoriented zones in the system, clearly visible by the distinct green and blue zones in Figs. 5(f) and 5(g).

In the final snapshot [$\varepsilon = 3.0$, Fig. 5(h)] there are two distinct orientations in the system, a main one along [433] (8° rotation from [111]) and a smaller grain [542] (rotated), separated by a boundary. Further analysis revealed a misorientation of approximately 14° between the two grains.

The rotation process can also be clearly identified from the insets of Figs. 5(c)–5(h). After the stress drop, a continuous distribution of orientations between [111] and [011] of the standard stereographic triangle emerged [inset Fig. 5(c)], followed by the appearance of two distinct orientations in the

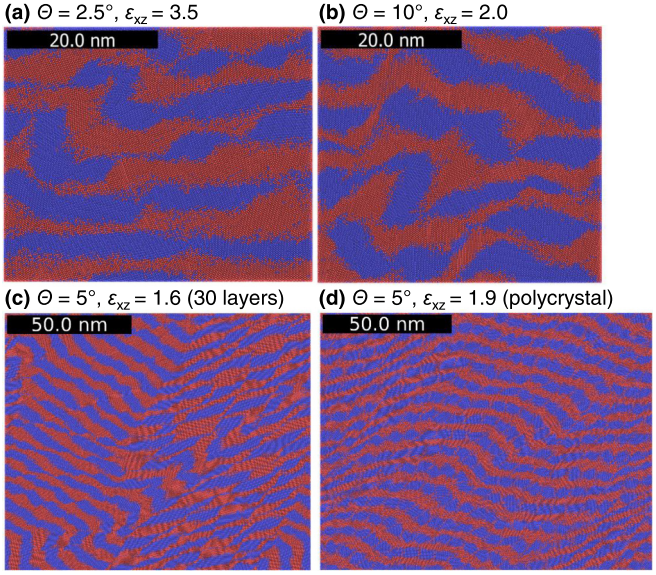

FIG. 6. Snapshots of various additional atomistic models. (a) System with $\theta = 2.5^\circ$ misorientation and 10 layers at a shear strain of $\varepsilon = 3.5$. (b) System with $\theta = 10^\circ$ misorientation and 10 layers at a shear strain of $\varepsilon = 2.0$. (c) System with $\theta = 5^\circ$ misorientation and 30 layers (a supercell of the smaller system) at a shear strain of $\varepsilon = 1.6$. (d) System with $\theta = 5^\circ$ misorientation and 30 polycrystalline layers after a shear strain of $\varepsilon = 1.9$. Atoms are color coded after their type; Cu atoms are shown in blue and Au atoms are shown in red.

insets of Figs. 5(c)–5(g). Finally at a shear strain of $\varepsilon = 3.0$ [inset Fig. 5(h)], the rotation had completed, i.e., all atoms in the system returned to an orientation close to [111].

We also evaluated the influence of lattice misorientation and system size. Figures 6(a) and 6(b) show snapshots of the calculations carried out with at a misorientation of $\theta = 2.5^\circ$ and $\theta = 10^\circ$ deformed using the aforementioned simple shear protocol. Figure 6(c) shows results for a larger supercell consisting of 30 layers, while Fig. 6(d) shows results for the most realistic of the systems investigated here, a polycrystalline nanolaminate. To set up the polycrystal, we chose hexagonal grains within each layer of lateral size identical to the layer thickness. The grains were randomly rotated around the z axis of our simulation cell (see Fig. 2 for the coordinate system). We observe comparable vortex patterns for all these systems. Figure 3(b) shows the stress-strain curve obtained for the supercell system of Fig. 6(c). Compared to the smaller systems, the large system showed the same yield stress and initially the same hardening, but the instability occurred at a smaller strain of $\varepsilon \approx 0.6$, compared to $\varepsilon \approx 1.3$ for the smaller system. Stress was comparable after the instability had occurred.

IV. DISCUSSION

The initial reduction of the averaged w^l_{RMS} in Fig. 3(a) during the equibiaxial tensile deformation can easily be connected to the layers co-deforming homogeneously. Even though co-deformation is here dictated by the periodic boundary conditions applied on the system, such behavior is observed experimentally under inhomogeneous loading conditions such as during nanoindentation of Cu|Au [45]. We note the inversion of the averaged w^l_{RMS} slope in Fig. 3(a) that corresponds to the appearance of roughness at the interfaces. Indeed during equibiaxial tensile deformation, where layers should thin down due to mass conservation, the only way to increase the averaged w^l_{RMS} value is for the layer to shear and therefore generate a rough interface. Such shear bands are visible in Fig. 1. This phenomenology of equibiaxial deformation seems to be independent of misorientation. Similar shear banding has been observed in different multilayered systems under indentation [46,47]. Roughness develops because materials do not deform continuously like in a laminar flow, but by slip on distinct glide planes [48]. Similar mechanisms have been reported for creating surface roughness at free surfaces [49] or buried interfaces [50] during deformation.

The first effect of misorientation between the shear direction and the {111} slip plane is an increase of yield stress with increasing misorientation θ during simple shear deformation (parallel to the initial x-y interface plane) in Fig. 3(b). As observed in previous work under parallel shear to the interface, fcc nanolaminates accommodate the deformation by interface sliding [34,51]. The higher resistance to shear therefore emerges because the interfacial shear strength increases: Any dislocation with a Burgers vector component normal to the interface that sits at the interface provides an obstacle to dislocation gliding parallel and along the interface. In order to accommodate for misorientation, steps must exist at the interfaces. The spacing between the steps is proportional to the misorientation angle θ. Thus, the steps disrupt the flat dislocation network at the interfaces and act as obstacles. This effect is amplified by the interface roughness that develops during the initial compression step. The dislocations are thus pinned, which prevents sliding of the interface. Zhang *et al.* [52] noted a similar behavior for the Cu|Nb system under simple shear parallel to the interface. Additionally, the local misorientation redirects the deformation away from the originally favored {111} plane. Dislocations on glide planes at an angle to the macroscopic shear direction experience a decrease in the resolved shear stress. This reduction in resolved shear stress is very small in the presently studied interfaces because of the small misorientation. However, together with stronger obstacles, it leads to an increase in the applied stress required for deformation, and because of the increase in obstacle density with deformation it also leads to strain hardening.

The second effect of misorientation is visible at larger shear strain. The stress drops for $\theta \neq 0^\circ$ in Fig. 3(b). This stress drop corresponds to the sudden increase of the averaged w^l_{RMS} in Fig. 3(a), which can be traced back to the appearance of waviness in the layer shapes as seen in Figs. 5(a)–5(h). The stress drops because of a burst of dislocations that cross several layers, with the two nucleation points shown by black arrows in Fig. 5(c). As the strain increases, dislocations continue to glide on successive planes, leading to the growth of a twinned area, in purple in Figs. 5(c)–5(g). This growth mechanism is compatible with twin growth from a grain boundary with the emission of partial dislocation on successive {111} planes [53]. In other words, strain hardening stops once localization of the deformation on an inclined plane releases some of the stored dislocations and stress.

These localized slip bands lead to the formation of multiple crystallites that further individually rotate until the next {111} plane is brought parallel to the macroscopic shear direction. Such formation of nanocrystalline material is often observed at interfaces in metallic sliding systems [54] or within shear bands that develop during bulk deformation [55]. (See Ref. [56] for a discussion of similarities between structural evolution at sliding interfaces and within shear bands.) The origin of the wave structure observed in the layer structure can be traced down to these localized slip bands. At larger strain, $\varepsilon > 2$, we attribute the plateau observed for w^l_{RMS} to folding of individual layers as the wavy structure is sheared [shown in Fig. 1(d)]. In that sense, the wavelike structures can be connected to the emergence of a nanocrystalline phase in the deformed material [25,54–58]. We see it in experiments because the interface between the two phases is initially straight and its deformation can be visualized in microscopy.

We have tested the relevance of the biaxial deformation to the overall mechanism by shearing directly the $\theta = 5^\circ$ system without performing the initial biaxial deformation. Just misaligning the lattice by an angle θ is not enough to trigger layer rotation and folding. In the context of the above discussion, this indicates that the shear bands and the associated interface roughness created during biaxial tensile deformation are necessary disturbances to create distinct obstacles at the interface and points of stress concentration. Indeed, qualitatively similar roughening is observed during the initial stages of the experiment [see Fig. 1(a)].

The supercell calculations revealed that the instability occurs at smaller strain as the system size increases. This indicates that strain hardening is mostly the result of a size effect acting only on "small" systems [59], indicating that the instability needs certain types of defects to nucleate. For a large realization of a nanolaminate, we would therefore expect that nucleation of plastic instabilities that lead to waves, folds, and vortices occurs at small strains, likely immediately upon plastic deformation. Note that even the strain required to cause such phenomena in our smallest cells are much smaller than the strains reported for a fluid-mechanical instability by Pouryazdan *et al.* [23].

V. SUMMARY AND CONCLUSIONS

We presented nonequilibrium molecular dynamics calculations of the deformation of Cu|Au nanolaminates. Our simulations reveal pattern formation during flow, namely the formation of waves, vortices, or swirls similar to those recently observed in sliding [9,10] and high-pressure torsion [23] experiments. We identify two crucial ingredients to stabilizing these patterns. First, we need rough bimaterial interfaces, here created by an initial equibiaxial compression step. Second, the {111} planes that accommodate slip in fcc Cu and Au need to be slightly misoriented with respect to the bimaterial interfaces. Both factors hinder dislocations from crossing the bimaterial interfaces. This leads to stress concentrations and the formation of crystallites of sizes on the order of the layer thickness that rotate as an alternative mechanism to accommodate strain. This rotation leads to the formation of waves that are folded by subsequent deformation. The instability occurs at small strain and is not of a fluid-mechanical nature, such as the often-quoted Kelvin-Helmholtz instability. It is rather intimately tied to the existence of a discrete crystal lattice that deforms by creation, annihilation, and motion of crystal defects.

ACKNOWLEDGMENTS

We thank C. Greiner and D. Rigney for helpful comments on the manuscript and Z. P. Luo for the SEM micrographs. The research was partially supported by the Helmholtz Association (Grant No. HCJRG-217) and the Deutsche Forschungsgemeinschaft DFG (Grant No. PA 2023/2). All our molecular dynamics calculations were carried out with LAMMPS [60]. ASE [61] and ovito [42] were used for preprocessing, postprocessing, and visualization. Computations were carried out on NEMO (University of Freiburg, DFG Grant No. INST 39/963-1 FUGG), ForHLR II (Steinbuch Center for Computing at Karlsruhe Institute of Technology, project "MULTILAYER"), and JUQUEEN (Jülich Supercomputing Center, project "hka18").

[1] B. M. Clemens, H. Kung, and S. A. Barnett, MRS Bull. **24**, 20 (1999).
[2] A. Misra and H. Krug, Adv. Eng. Mater. **3**, 217 (2001).
[3] L. B. Freund and S. Suresh, *Thin Film Materials: Stress, Defect Formation and Surface Evolution* (Cambridge University, Cambridge, England, 2004).
[4] A. Gola and L. Pastewka, Lubricants **7**, 44 (2019).
[5] M. M. Khruschov, Wear **28**, 69 (1974).
[6] D. A. Rigney and J. P. Hirth, Wear **53**, 345 (1979).
[7] M. Mishra and I. Szlufarska, Tribol. Lett. **45**, 417 (2012).
[8] M. Mishra, P. Egberts, R. Bennewitz, and I. Szlufarska, Phys. Rev. B **86**, 045452 (2012).
[9] Z.-P. Luo, G.-P. Zhang, and R. Schwaiger, Scr. Mater. **107**, 67 (2015).
[10] E. Cihan, H. Störmer, H. Leiste, M. Stüber, and M. Dienwiebel, Sci. Rep. **9**, 9480 (2019).
[11] H. J. Kim, S. Karthikeyan, and D. Rigney, Wear **267**, 1130 (2009).
[12] D. A. Rigney and S. Karthikeyan, Tribol. Lett. **39**, 3 (2010).
[13] X.-Y. Fu, M. L. Falk, and D. A. Rigney, Wear **250**, 420 (2001).
[14] X.-Y. Fu, D. A. Rigney, and M. L. Falk, J. Non-Cryst. Solids **317**, 206 (2003).
[15] J. H. Wu, S. Karthikeyan, M. L. Falk, and D. A. Rigney, Wear **259**, 744 (2005).
[16] S. Odunuga, Y. Li, P. Krasnochtchekov, P. Bellon, and R. S. Averback, Phys. Rev. Lett. **95**, 045901 (2005).
[17] Y. Ashkenazy, N. Q. Vo, D. Schwen, R. S. Averback, and P. Bellon, Acta Mater. **60**, 984 (2012).
[18] J. Zhou, R. S. Averback, and P. Bellon, Acta Mater. **73**, 116 (2014).
[19] S. Li, L. Pastewka, and P. Gumbsch, Acta Mater. **165**, 577 (2019).

[20] Hermann von Helmholtz, Ber. Akad. Wiss. Berlin, 215 (1868).
[21] W. Thompson, Philos. Mag. **42**, 362 (1871).
[22] S. A. Thorpe, J. Fluid Mech. **46**, 299 (1971).
[23] M. Pouryazdan, B. J. P. Kaus, A. Rack, A. Ershov, and H. Hahn, Nat. Commun. **8**, 1611 (2017).
[24] A. Emge, S. Karthikeyan, H. J. Kim, and D. A. Rigney, Wear **263**, 614 (2007).
[25] P. Stoyanov, P. A. Romero, T. T. Järvi, L. Pastewka, M. Scherge, P. Stemmer, A. Fischer, M. Dienwiebel, and M. Moseler, Tribol. Lett. **50**, 67 (2013).
[26] K. Minowa and K. Sumino, Phys. Rev. Lett. **69**, 320 (1992).
[27] L. Pastewka, S. Moser, P. Gumbsch, and M. Moseler, Nat. Mater. **10**, 34 (2011).
[28] G. Moras, A. Klemenz, T. Reichenbach, A. Gola, H. Uetsuka, M. Moseler, and L. Pastewka, Phys. Rev. Mater. **2**, 083601 (2018).
[29] W. M. Paulson and J. E. Hilliard, J. Appl. Phys. **48**, 2117 (1977).
[30] K. Fitzner, Q. Guo, J. Wang, and O. J. Kleppa, J. Alloys Compd. **291**, 190 (1999).
[31] J. A. Borders, Thin Solid Films **19**, 359 (1973).
[32] G. P. Zhang, Y. Liu, W. Wang, and J. Tan, Appl. Phys. Lett. **88**, 013105 (2006).
[33] A. Gola and L. Pastewka, in *NIC Symposium 2018*, NIC Series (Forschungszentrum Jülich GmbH, Jülich, 2018), Vol. 49, pp. 247–254.
[34] A. Gola, G.-P. Zhang, L. Pastewka, and R. Schwaiger, MRS Commun. **9**, 1067 (2019).
[35] Y. Mishin, M. J. Mehl, D. A. Papaconstantopoulos, A. F. Voter, and J. D. Kress, Phys. Rev. B **63**, 224106 (2001).
[36] G. Grochola, S. P. Russo, and I. K. Snook, J. Chem. Phys. **123**, 204719 (2005).
[37] A. Gola and L. Pastewka, Modell. Simul. Mater. Sci. Eng. **26**, 055006 (2018).
[38] H. J. C. Berendsen, J. P. M. Postma, W. F. van Gunsteren, A. DiNola, and J. R. Haak, J. Chem. Phys. **81**, 3684 (1984).
[39] H. C. Andersen, J. Chem. Phys. **72**, 2384 (1980).
[40] M. Parrinello and A. Rahman, J. Appl. Phys. **52**, 7182 (1981).
[41] P. M. Larsen, S. Schmidt, and J. Schiøtz, Modell. Simul. Mater. Sci. Eng. **24**, 055007 (2016).
[42] A. Stukowski, Modell. Simul. Mater. Sci. Eng. **18**, 015012 (2010).
[43] M. L. Falk and J. S. Langer, Phys. Rev. E **57**, 7192 (1998).
[44] F. Shimizu, S. Ogata, and J. Li, Mater. Trans. **48**, 2923 (2007).
[45] X. Li, T. Kreuter, X. M. Luo, R. Schwaiger, and G. P. Zhang, Mater. Res. Lett. **5**, 20 (2017).
[46] Y. P. Li, X. F. Zhu, G. P. Zhang, J. Tan, W. Wang, and B. Wu, Philos. Mag. **90**, 3049 (2010).
[47] J. W. Yan, X. F. Zhu, G. P. Zhang, and C. Yan, Thin Solid Films **527**, 227 (2013).
[48] M. Zaiser, Adv. Phys. **55**, 185 (2006).
[49] A. R. Hinkle, W. G. Nöhring, and L. Pastewka, arXiv:1901.03236.
[50] P. Bellon and R. S. Averback, Phys. Rev. Lett. **74**, 1819 (1995).
[51] A. Gola, P. Gumbsch, and L. Pastewka, Acta Mater. **150**, 236 (2018).
[52] R. F. Zhang, I. J. Beyerlein, S. J. Zheng, S. H. Zhang, A. Stukowski, and T. C. Germann, Acta Mater. **113**, 194 (2016).
[53] P. M. Anderson, J. P. Hirth, and J. Lothe, *Theory of Dislocations* (Wiley & Sons, New York, 2017).
[54] P. Heilmann, W. A. T. Clark, and D. A. Rigney, Acta Metall. **31**, 1293 (1983).
[55] M. Hatherly and A. S. Malin, Scripta Metall. **18**, 449 (1984).
[56] D. A. Rigney, X. Y. Fu, J. E. Hammerberg, B. L. Holin, and M. L. Falk, Scr. Mater. **49**, 977 (2003).
[57] X. Chen, Z. Han, and K. Lu, Wear **320**, 41 (2014).
[58] J. B. Singh, J. G. Wen, and P. Bellon, Acta Mater. **56**, 3053 (2008).
[59] M. F. Horstemeyer, M. I. Baskes, and S. J. Plimpton, Acta Mater. **49**, 4363 (2001).
[60] S. Plimpton, J. Comput. Phys. **117**, 1 (1995).
[61] A. Hjorth Larsen *et al.*, J. Phys. Condens. Matter **29**, 273002 (2017).